DOI

ACCURATE OPTICAL OBSERVATIONS ON LOW EARTH ORBIT SATELLITES DURING THE MAY 2024 SEVERE SOLAR STORM: ANALYSIS OF THE O-C VALUES AND THEIR CAUSES

RADU DANESCU[1], PAUL DOLEA[2], VLAD TURCU[3], MIHAIL BARBOSU[4]

[1]*Technical University of Cluj-Napoca, Cluj-Napoca, Romania*
Email: radu.danescu@cs.utcluj.ro
Corresponding author: Tel: +40 264 401457
[2]*Technical University of Cluj-Napoca, Cluj-Napoca, Romania*
[3]*Romanian Academy, Astronomical Observatory Cluj-Napoca, Cluj-Napoca, Romania*
[4]*Rochester Institute of Technology, Rochester, NY, USA*

Abstract. In May, 2024 took place a severe solar storm with strong geomagnetic storm components. Based on optical observation of low Earth orbit (LEO) satellites during and after the solar event, we describe and make available a database featuring topocentric observations for more than 300 LEOs, and present the analysis of the storm's impact on the satellites' orbital positions.

Between May 10 and May 15, on several nights, we performed a series of observations on LEOs from Cluj-Napoca, Romania, and the Feleacu Station of the Astronomical Observatory Cluj-Napoca. Two instruments were used: a wide Field of View instrument based on an 85 mm lens with a DSLR camera, and a narrow Field of View instrument based on an Orion ShortTube 80 refractor telescope, with a SBIG STT 1603ME CCD camera. These observations were gathered in a database with information about the instrument used and location, the satellite's identifier, time of observation, and the topocentric position. This database contains over 300 satellites.

In the second part of this study, we used these observations to compare the observed apparent positions with the predicted positions computed from the up-to-date Two-Line Elements (TLEs), available in the USSPACECOM catalog. An initial investigation of this comparison leads us to identify satellites that underwent active space maneuvers (ASM), with most satellites belonging to the Starlink constellation.

Additionally, we plotted and investigated the distribution of O-C values for ASM and non-space maneuvered (NSM) satellites during the solar storm. Among all surveyed satellites, prediction errors for ASM satellites were significantly larger when compared to NSM satellites. These differences are illustrated in plots of ASM versus NSM satellites.

We found that O-C errors were driven primarily by active maneuvers, rather than by the G5 geomagnetic storm itself.

Key words: Solar storm – Optical surveillance – LEOs – O-C analysis.

1. INTRODUCTION

Solar activity, manifested in terms of solar spots, F10.7cm radio flux, solar flares and Coronal Mass Ejections (CMEs), showed a significant increase from 2021

to 2024, which is typical to a rising branch and a maximum solar activity cycle. However, the solar activity during this time-period is exceeded and outrun the previous model-based predictions; this is shown in Figure 1 (NOAASWPC, 2025).

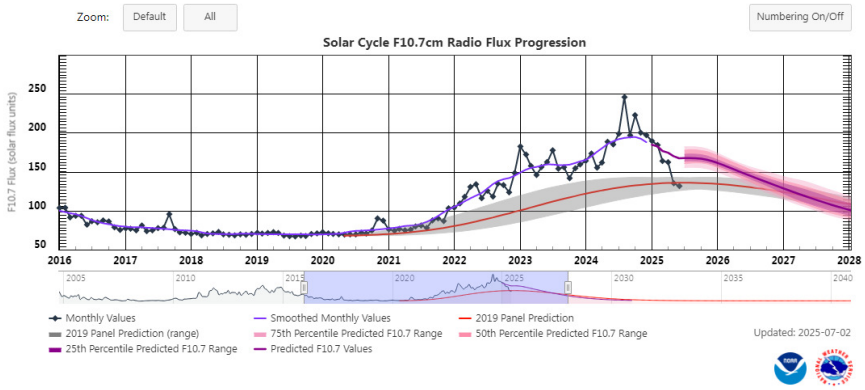

Fig. 1 – The Radio Flux Progression F10.7cm for the current solar cycle, with a May 2024 monthly value of 188.37 Solar Flux Unit, positioned on the increasing branch of the maximum (from NOAASWPC, 2025).

When solar activity increases, powerful solar wind disrupts the Earth's magnetosphere, and consequently geomagnetic storm occurs. Between May 10 and May 12, 2024, a geomagnetic storm of a G5-level took place, which was the most intense event in more than two decades. This event produced aurorae at latitudes far lower than usual, in both the Northern and Southern hemispheres.

An overview of the May 2024 G5-level geomagnetic storm is given in (Kwak et al., 2024). The main causes of the G5-level geomagnetic storm were a series of 11 major X-class solar flare events originated in the complex sunspot cluster designated by the National Oceanic and Atmospheric Administration (NOAA) as active regions (ARs) 13664 and 13668, between 2024/05/08 04:37 UT and 2024/05/14 17:02 UT. Moreover, the severe features of the geomagnetic storm started on 2024/05/10 17:05 UT and were caused by the arrival of the combined multiple interplanetary CME (ICME) and interplanetary magnetic field (IMF) intensity, associated with a sharp increase in proton density and solar wind speed. The study (Kwak et al., 2024) emphasizes the impact of this event on Earth's magnetosphere and upper atmosphere, strong auroral activity, thermosphere heating, and changes in the global atmospheric composition and ionosphere.

The solar activity influences the behavior of satellites in orbits due to its effect on the upper layers of the Earth's atmosphere. LEOs are especially vulnerable, as they experience more atmospheric friction, and in order to maintain their altitude

they often need to perform space maneuvers.

A paper by (Oliveira and Zestra, 2019) investigates the effects of atmospheric air drag forces driven by geomagnetic storms caused by CME on the orbital decays of LEOs, for a time span longer than a Solar Cycle. It includes data from two LEOs: the CHAllenge Mini-satellite Payload (CHAMP) and the Gravity Recovery And Climate Experiment (GRACE). The study finds that orbital drag effects are larger for lower altitudes (CHAMP) when compared with GRACE (higher altitudes). Moreover, drag effects manifest first at higher latitudes and for extreme storms, stronger orbital drag effects occur during the early phase at low/equatorial latitudes, due to heating propagation from high latitudes. Another important finding is that the increase in storm intensity determined an increase in storm time orbital decay along the satellites' path.

Space weather events, especially solar flares, can have disastrous consequences on the satellites orbiting the Earth. For example, the CME of February 2022 caused the reentry of 38 Starlink satellites. The cause, as presented in (Kataoka, 2022), is not solely the severity of the space weather event, but the incorrect model-based estimation of the arrival of the solar wind, which led to the approval of the satellites' launches instead of a decision to postpone the launch.

A recent study (Parker, 2024), published in the wake of the May 2024 G5-level event, highlights the main problems related to LEO orbit prediction in the case of such events. The authors perform a bulk analysis on LEOs' orbital elements and find that while many orbits decayed as expected, there were also multiple maneuvers, mostly performed by the Starlink constellation, to correct the position in orbit.

Another study dedicated to the effects of the May 2024 G5-level event, focuses on an Indonesian GEO satellite (Pratiwi et al., 2025) and finds that all orbital elements were affected. The semi-major axis, eccentricity and mean-anomaly were rapidly affected by the storm's main phase, whereas the inclination, right ascension of the ascending node and the argument of perigee had a gradual or even a delayed response.

When the G5 geomagnetic storm was forecasted on May 10, we started an optical space surveillance campaign on LEOs, in order to create a relevant database of topocentric observations and use it in evaluating the influence of this G5-level event on LEOs' positions.

2. MATERIALS AND METHODS

2.1. INSTRUMENTS

Our observations were performed using two optical instruments with different field of view (FOV): a real-time, portable, wide FOV instrument deployed in Cluj-Napoca, and a narrow FOV instrument deployed at the Feleacu Station of the

Astronomical Observatory Cluj-Napoca.

The wide FOV system had a Canon EOS 800 D DSLR camera equipped with an 85 mm focal length Canon EF 85mm f/1.8 USM lens. The image size was set at 2400×1600 pixels, leading to an angular pixel size of 23 arcseconds/pixel. The camera was synchronized by an external trigger signal based on a GPS receiver, to ensure precise synchronization with the global UTC time. The effective FOV of the system was 15×10 degrees. The process of image acquisition, image processing, astrometric calibration, and astrometric reduction followed by the generation of the Tracking Data Message (TDM) file (CCSDS, 2007) was performed in real-time, on a 13-inch MacBook Pro 2020, equipped with the Apple Silicon M1 processor.

The narrow FOV instrument was equipped with an Orion ShortTube 80 refractor telescope and an SBIG STT 1603ME CCD camera (SBIG, 2015), working in binning mode, producing 16-bit FITS images of 768×512 pixels in size. The telescope was mounted on a PlaneWave L600 (PlaneWave, 2019a, 2019b) fast-moving accurate equatorial mount. The acquisition system was synchronized using a Synoptes precise timestamping device, GPS/Galileo - based, able to assign microsecond-accurate timestamps to the acquired images (Balan et al, 2023). The effective FOV of the system was 1.98×1.32 degrees. Images from the narrow FOV instrument were processed offline, using the same algorithms as the ones used for the wide FOV. Observational errors were periodically evaluated for the narrow FOV sensor during calibration campaigns for LEOs.

More details about the instruments are available in (Danescu, 2024) and (Danescu, 2022).

2.2. IMAGE PROCESSING

Image files were processed during acquisition (online processing) for the wide FOV instrument and after acquisition (offline processing) for the narrow FOV instrument. The image processing algorithms used in both scenarios were identical and involved the following steps:

1. Conversion to grayscale: transforming the color image to grayscale.

2. Background estimation and removal: using a large-size median filter for background estimation to avoid the need for a specific polynomial surface model, and then the estimating the background by subtracting from the grayscale image.

3. Image differencing: calculating the differences between successive frames after background removal, to detect moving objects. All LEOs showed apparent motion, visible in the difference image. A very low threshold (1-2 intensity points) was applied, to generate a binary image.

4. Connected components labeling: identifying and labeling connected regions in the difference binary image, as potential streaks.

5. Identification of elongated shapes: evaluating the geometrical properties of the connected regions to find the center of mass, orientation angle, eccentricity, length, and area. Regions with high eccentricity, area, and length above a certain threshold were selected as streak candidates, eliminating many false positives caused by cloud motion, star motion in staring mode, or condensation trails of airplanes.

6. Tracklet formation and validation: merging streak candidates with similar orientations and aligned centers of mass on the same trajectory, further reducing false positives.

7. Astrometric calibration and reduction: tools from astrometry.net (Lang, 2010), freely available on all Unix-based platforms, including Mac OS, were used for obtaining the relationship between the pixel coordinates and the topocentric equatorial coordinates. For the real-time operation, a calibration grid was formed, based on fusion of multiple calibration results, so that at each instant a filtered result could be used for astrometric reduction. More details are presented in (Danescu, 2024).

2.3. COMPUTATION OF ERRORS BETWEEN THE OBSERVED AND CATALOG-BASED PREDICTED POSITIONS (O-C)

Astrometric results for both real time and offline processing modes were generated in the form of TDM files, containing observed topocentric J2000 equatorial coordinates - Right Ascension ($\mathrm{RA_{obs}}$) and Declination ($\mathrm{Dec_{obs}}$) - of the center of the streaks caused by the observed targets, timestamped with the UTC time of the middle of the exposure process.

Predicted apparent topocentric coordinates for LEOs corresponding to observation timestamps, Right Ascension ($\mathrm{RA_{calc}}$) and Declination ($\mathrm{Dec_{calc}}$), were generated with Orekit library (Orekit, 2024) using the latest TLE catalog data. TLEs were downloaded from space-track.org on the day of the observation, right before starting the acquisition process. The Orekit library contains the SGP4/SDP4 propagator algorithm, which uses orbital elements available from TLE files, to accurately predict the position of an object in Earth's orbit.

With the observed and the predicted topocentric coordinates we started an analysis of the corresponding apparent trajectories. First, for each observed datapoint we obtained ($\mathrm{S_a}$, $\mathrm{W_a}$), the apparent angular coordinates in the (S,W) radial-transverse-normal (RSW) satellite coordinate system, on the predicted orbit (Vallado, 2013). Then, with the $\mathrm{S_a}$ coordinates we computed the angular Along Track Errors (ATEa), and these led to the angular distance between the observed and predicted points. Furthermore, the apparent angular velocity $\mathrm{V_{Sa}}$ was determined for each point on the predicted path, and the O-C time differences were derived.

If the processing is done in real time, as in the case of the Wide FOV system, the comparison between the predicted positions and the detected positions is also done in real time, as shown in Figures 2 and 3.

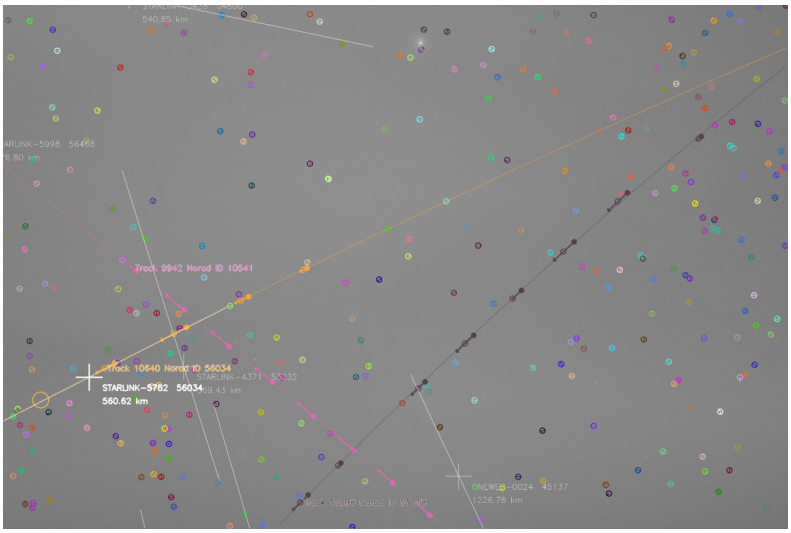

Fig. 2 – Image generated during real time operation of the wide FOV sky surveillance system, May 11, 2024. The colored trajectories are detected tracklets in image coordinates, and the white trajectories are the predicted satellite trajectories based on orbital information. In this image, we can see that the Starlink 5782 satellite's actual position seems to fall behind its predicted position (white cross).

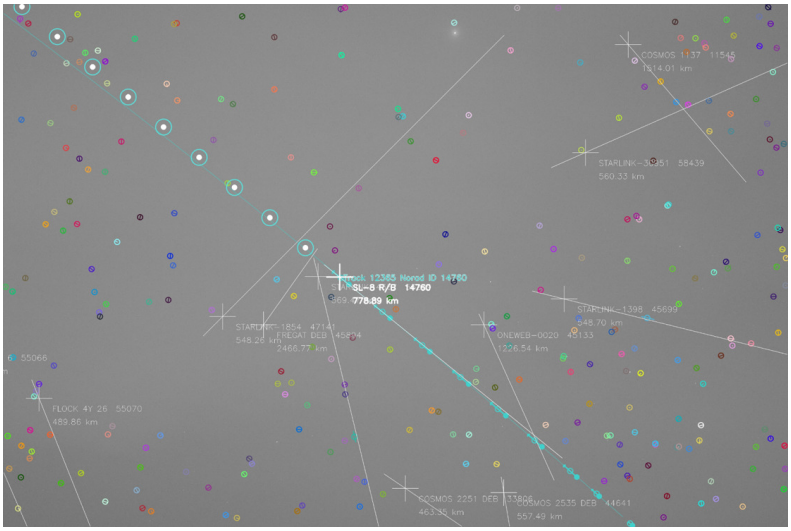

Fig. 3 – Image generated during real time operation of the sky surveillance system, May 11, 2024. The colored trajectories are detected tracklets in image coordinates, and the white trajectories are the predicted satellite trajectories based on orbital information. In this image, we can see that the predicted position of the SL-8 R/B space debris (white cross) matches the position of the detection.

2.4. DATA ANALYSIS

Data analysis was focused on two directions: the analysis of the O-C errors for all observed satellites for all observation sessions, correlated with the satellite's elevation, and the identification of the maneuvers as additional sources of errors. In plotting the errors versus elevation, we expected to see a clear influence of the solar storm on lower elevation satellites, and a lesser influence on higher satellites.

The O-C error analysis was based on our observation data, compared with the latest orbital parameters.

The discrimination between active space maneuvers (ASM) satellites and no space maneuvered (NSM) satellites was based on the evolution of the mean orbital period during the month of May 2024, using the TLEs available in the USSPACECOM catalog. A sudden increase in the mean orbital period was the criterion used for identifying ASM satellites. We performed the following steps:

- We downloaded TLE series for all the identified satellites covering the period 2024.05.01 – 2024.05.25, form https://www.space-track.org/.
- We downloaded the kp values series from Geomagnetic Observatory Niemegk, GFZ German Research Centre for Geosciences, Potsdam, Germany. (ftp://ftp.gfz-potsdam.de/pub/home/obs/Kp_ap_Ap_SN_F107), and we transformed to ap series using the kp-ap conversion table.
- We plotted the orbital elements series for each satellite along with superposed ap index during the above-mentioned time interval. Satellites mean period time series were exemplified in Figures 4, 5 and 6. We considered the mean period time series a sensitive plot for visual identifying of G5 geomagnetic disturbances and for station keeping maneuvers.
- The visual maneuver identification process identified positive step-increasing in mean period, with threshold values depending on the satellite elevation - average of the perigee and apogee distances.

On Figure 4, we see that on May 11, 2024, before the active maneuver, there was a sudden decrease of the mean period due to the G5 solar storm; immediately thereafter, a *station keeping* maneuver was executed with the objective of preserving the satellite's elevation, which is reflected as an adjustment in the mean period. This plot is representative for most Starlink satellites. This satellite has a mean elevation of around 560 km; at this altitude the effect of the solar event is significant.

Figure 5 shows that starting on May 11, the mean period of the satellite decreased, due to the G5 storm. On May 20, a strong active maneuver on the satellite resulted in a sharp increase in the mean period, to a level exceeding the one observed

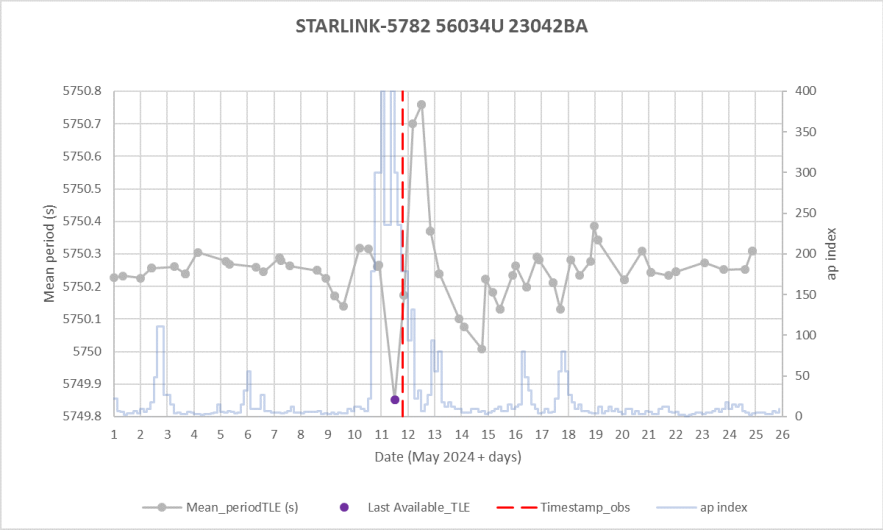

Fig. 4 – Example of an ASM satellite orbital behavior with an active maneuver on May 11, 2024.
Legend: in blue - solar activity; gray - mean period vs time; red - moment of optical observation; purple - TLE epoch before, and closest to observation time, used for O-C computation.

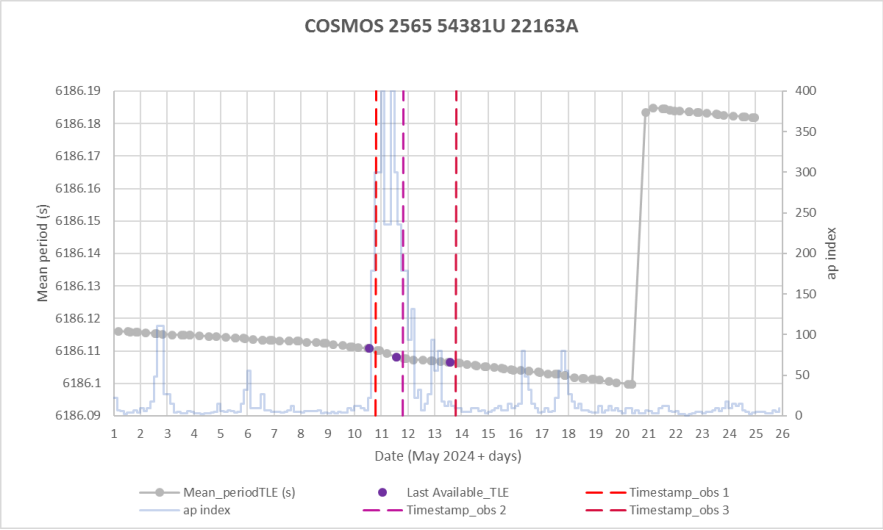

Fig. 5 – Example of an NSM satellite orbital behavior during May 10 - May 20, 2024, followed by an active maneuver on May 20, 2024.
Legend: in blue - solar activity; gray - mean period vs time; red - moment of optical observation; purple - TLE epoch before, and closest to observation time, used for O-C computation.

prior to the solar event. The mean elevation of this satellite is around 900 km; at this altitude the effect of the solar event is not as strong as it is on satellites at lower altitudes.

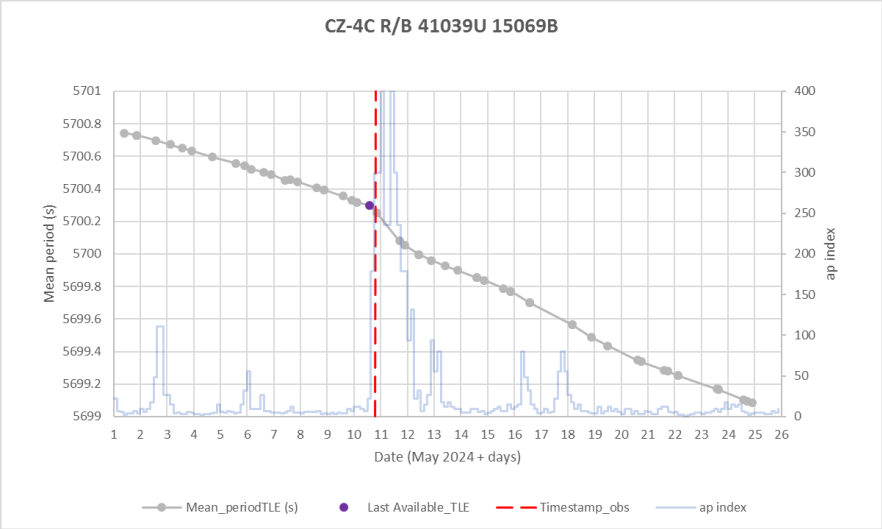

Fig. 6 – Example of an NSM satellite (rocket body-debris) orbital behavior throughout the study interval.
Legend: in blue - solar activity; gray - mean period vs time; red - moment of optical observation; purple - TLE epoch before, and closest to observation time, used for O-C computation.

Figure 6 depicts the behavior of a typical NSM satellite. This satellite has a mean elevation of approximately 500 km - comparable to that of Starlink satellites, meaning that the solar event significantly affected its orbital behavior, manifested as a steep reduction in the mean period throughout the observation interval.

3. RESULTS

During our observation campaign we detected and validated a total number of 334 distinct satellites, as shown in Table 1 and Table 2.

Table 1

Number of satellites detected each observing session with the narrow FOV system

Observation Date	NSM	ASM	ALL
2024.05.10	19	48	67
2024.05.13	8	30	38
2024.05.15	10	17	27

Table 2

Number of satellites detected each observing session with the wide FOV system

Observation Date	NSM	ASM	ALL
2024.05.10	25	41	66
2024.05.11	14	19	33
2024.05.13	39	81	120

In what follows, we present successive graphs, generated using a narrow and a wide field of view (FOV), respectively. These plots illustrate the distributions of ASM and NSM satellites over the observation period and are followed by tables containing a concise statistical analysis, which includes the mean and standard deviation of the O-Cs.

The narrow FOV system was used on May 10 (Figure 7), May 13 (Figure 8), and May 15 (Figure 9), for LEOs, as part of the EUSST program, not just for analyzing the behavior of satellites following the solar event; here, images were processed offline. The mean and standard deviation of the O-Cs for the narrow FOV system are shown in Table 3.

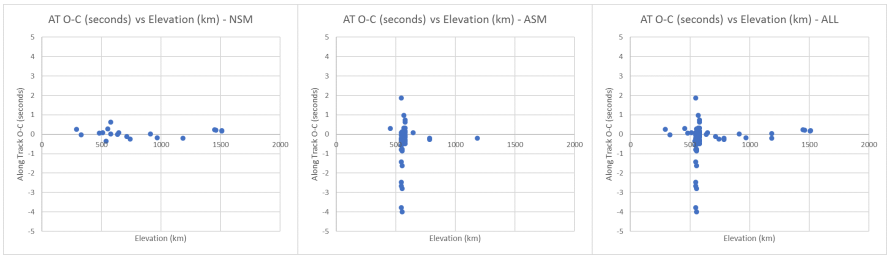

Fig. 7 – Observations with the narrow FOV system on 2025.05.10: left: distribution of O-Cs vs elevation for NSM observed satellites; center: distribution of O-Cs vs elevation for ASM observed satellites; right: distribution of O-Cs vs elevation for all observed satellites.

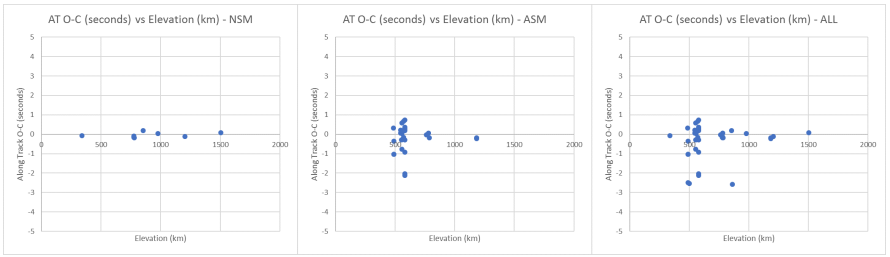

Fig. 8 – Observations with the narrow FOV system on 2025.05.13: left: distribution of O-Cs vs elevation for NSM observed satellites; center: distribution of O-Cs vs elevation for ASM observed satellites; right: distribution of O-Cs vs elevation for all observed satellites.

Table 3

Statistical results summarizing the narrow FOV

	NSM		ASM		ALL	
Observation Date	O-C Mean Absolute (seconds)	O-C Standard Deviation (seconds)	O-C Mean Absolute (seconds)	O-C Standard Deviation (seconds)	O-C Mean Absolute (seconds)	O-C Standard Deviation (seconds)
2024.05.10	0.1739	0.2267	0.6984	1.0792	0.6535	1.0348
2024.05.13	0.1186	0.1319	0.5061	0.7119	0.4263	0.6305
2024.05.15	0.1540	0.1939	0.4188	0.3083	0.3180	0.3121

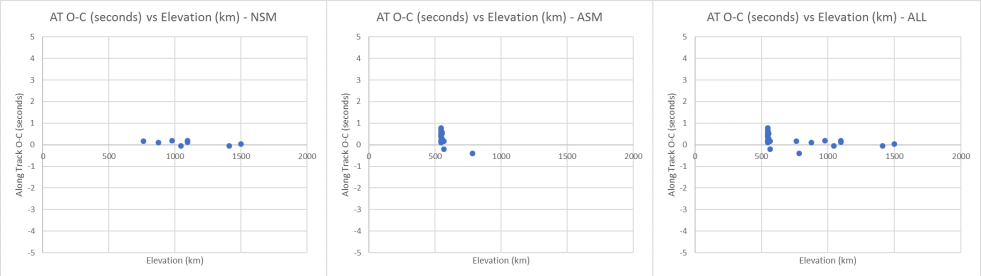

Fig. 9 – Observations with the narrow FOV system on 2025.05.15: left: distribution of O-Cs vs elevation for NSM observed satellites; center: distribution of O-Cs vs elevation for ASM observed satellites; right: distribution of O-Cs vs elevation for all observed satellites.

The wide FOV system was used on May 10 (Figure 10), 2024, May 11 (Figure 11), 2024, and May 13 (Figure 12), 2024, images being processed online. On May 12, the sky in the Cluj-Napoca area was too cloudy for LEO observations. The mean and standard deviation of the O-Cs for the wide FOV system are shown in Table 4.

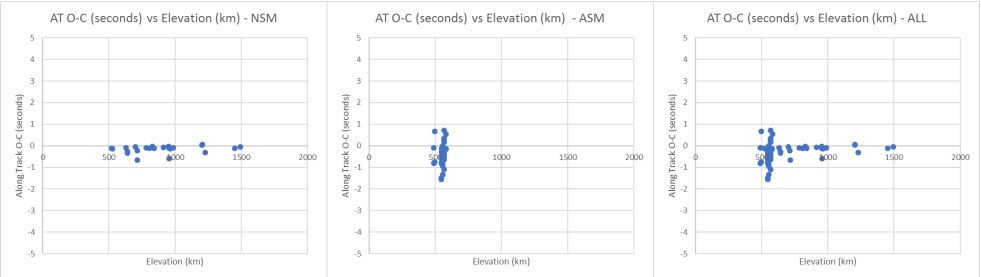

Fig. 10 – Observations with the wide FOV system on 2025.05.10: left: distribution of O-Cs vs elevation for NSM observed satellites; center: distribution of O-Cs vs elevation for ASM observed satellites; right: distribution of O-Cs vs elevation for all observed satellites.

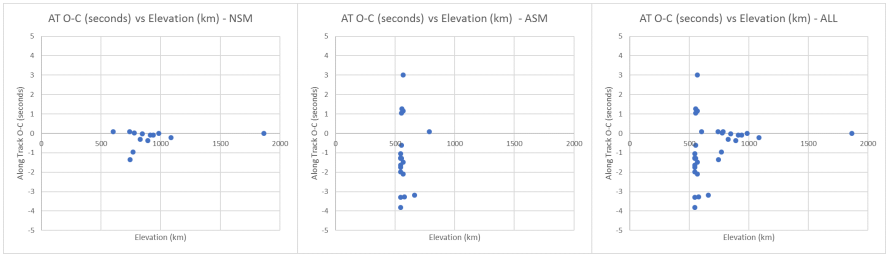

Fig. 11 – Observations with the wide FOV system on 2025.05.11: left: distribution of O-Cs vs elevation for NSM observed satellites; center: distribution of O-Cs vs elevation for ASM observed satellites; right: distribution of O-Cs vs elevation for all observed satellites.

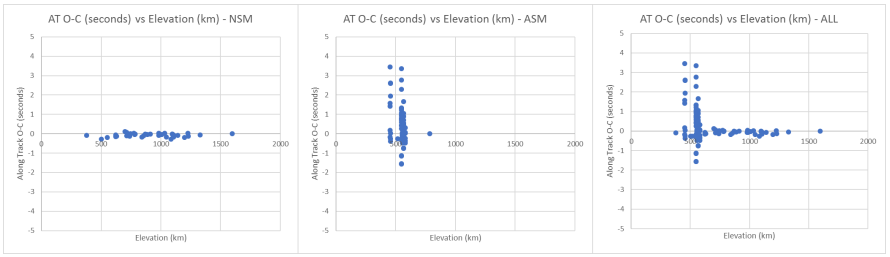

Fig. 12 – Observations with the wide FOV system on 2025.05.13: left: distribution of O-Cs vs elevation for NSM observed satellites; center: distribution of O-Cs vs elevation for ASM observed satellites; right: distribution of O-Cs vs elevation for all observed satellites.

In addition to the above statistical results, we were also able to observe the effect of the solar storm on the O-Cs values for several individual satellites. Three satellites were observed in two different days, on May 11 and on May 13: Starlink-1636, Starlink-5782, and Starlink-5793, belonging to the ASM group. The O-C comparisons are shown in Figures 13, 14 and 15, which clearly show that the errors on May 11 were significantly higher than the ones on May 13.

We have managed to detect a single satellite in all three sequences: Cosmos-2565, an object belonging to the NSM group. The O-Cs in Figure 16 show that even though the May 11 sequence shows larger errors, they are still very small compared to the ASM satellites. This object is at a higher elevation, over 900 km above the Earth surface.

Table 4

Statistical results summarizing the wide FOV

	NSM		ASM		ALL	
Observation Date	O-C Mean Absolute (seconds)	O-C Standard Deviation (seconds)	O-C Mean Absolute (seconds)	O-C Standard Deviation (seconds)	O-C Mean Absolute (seconds)	O-C Standard Deviation (seconds)
2024.05.10	0.2920	0.6363	0.5226	0.5391	0.4325	0.5752
2024.05.11	0.2738	0.4383	1.7349	1.7882	1.0957	1.4446
2024.05.13	0.2028	0.6326	0.6930	0.9699	0.5309	0.9044

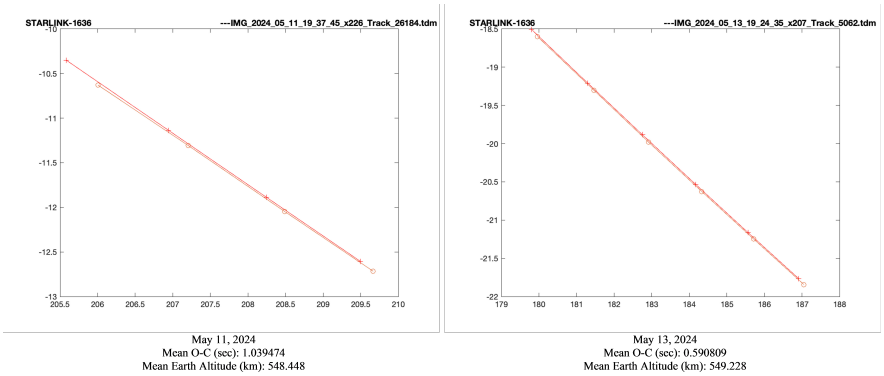

Fig. 13 – Comparison between observed (o) and computed (+) positions for Starklink-1636, on May 11 and May 13, 2024.

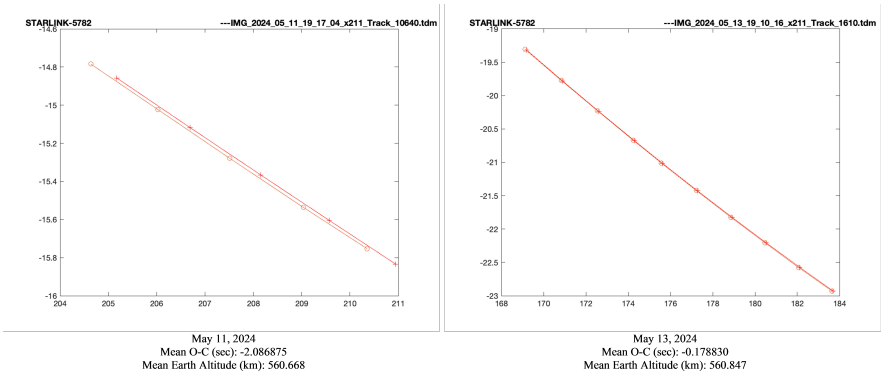

Fig. 14 – Comparison between observed (o) and computed (+) positions for Starklink-5782, on May 11 and on May 13.

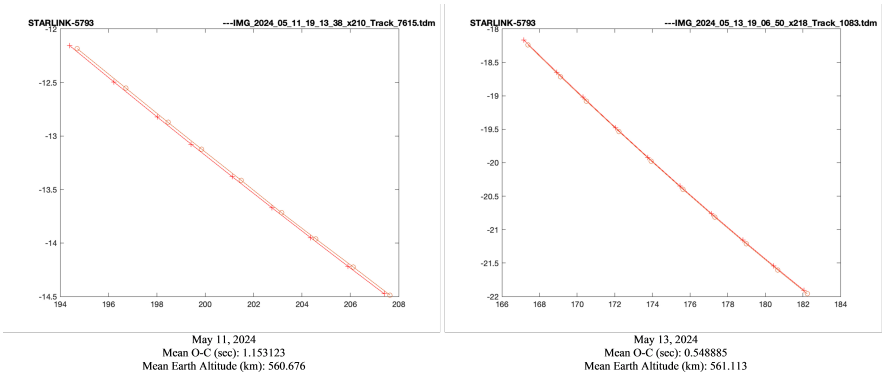

Fig. 15 – Comparison between observed (o) and computed (+) positions for Starklink-5793, on May 11 and on May 13.

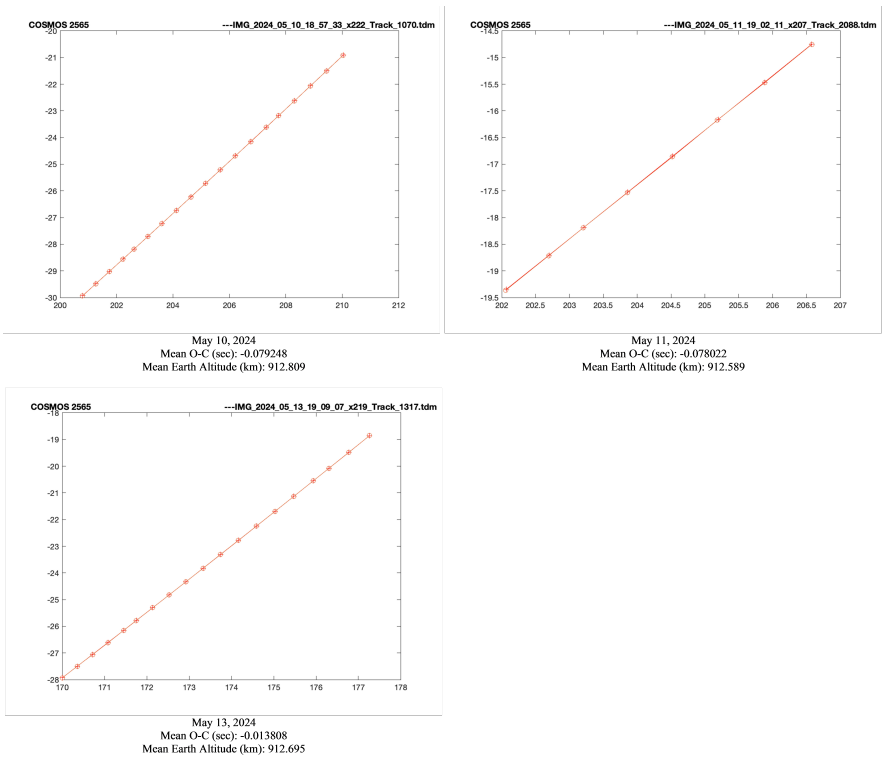

Fig. 16 – Comparison between observed (o) and computed (+) positions for Cosmos-2565, on May 10, May 11 and May 13.

4. DISCUSSION

The results from the three observation sessions with the Wide FOV system show that the errors on May 11, after the full effect of the solar explosion, are significantly larger than the errors on May 10, and on May 13. The narrow FOV observations did not include May 11, but they still showed an increase in errors between May 10 and May 13, followed by a gradual decrease.

From the above figures and corresponding tables, one can see that the O-C errors do not appear to be correlated with the satellite's elevation for the NSM satellites and they are much lower than the ones for the ASM satellites. For the ASM satellites, one can observe two elevation clusters, one around 470 km and one around 560 km; these are the two main orbit elevation values for the Starlink family.

On May 10 and May 13, observations were made with both the narrow and wide the FOV systems. On May 10, one can see larger differences between the two systems, because observations were performed at different times. Wide FOV observations were performed earlier (between 18:40-19:20 UTC), before the full effect of the solar storm were felt, while the narrow FOV observations were performed later (after 22:10 UTC), when the effect of the solar storm was apparent on the atmosphere, and even an aurora was visible.

5. CONCLUSIONS

This paper presents the results of a four-day series of observations on LEOs, conducted after the announcement of the May 10 solar storm. The observations involved two optical instruments, a real time, wide FOV portable instrument, and a narrow FOV instrument of higher accuracy. These observations were gathered in a database with information on the instrument used and location, the satellite's identifier, time of observation, and the topocentric position. This database contains 334 satellites.

In the second part of this study, these observations were used to compare the measured apparent positions with the predicted positions derived from the up-to-date Two-Line Elements (TLEs) provided in the USSPACECOM catalog. While the experiment was performed in less-than-ideal conditions, in urban and near urban settings and with a moderately clouded sky, we have observed a severe increase in the O-C values for multiple LEO satellites, especially the ASM ones, which includes many from the Starlink family. Our analysis indicates that the primary source of the observed O-C errors arises from active satellite maneuvers – conducted either in anticipation of, or in response to, the G5 geomagnetic storm – rather than from the direct effects of the storm itself.

Future work will be dedicated to the development of a satellite propagation

model, based on machine learning, that can integrate the space weather information, can also detect maneuvers using observation data, and include the maneuvers and space weather information in the prediction of the satellite's position in the future. A similar work, presented in (Brandt, 2020), estimates the changes in atmospheric density using observed trajectories of known satellites, but do not take into consideration unexpected maneuvers. The main challenge will be to acquire a vast amount of observation data to train the model.

Acknowledgements. This work is supported by the project "Romanian Hub for Artificial Intelligence-HRIA", Smart Growth, Digitization and Financial Instruments Program, MySMIS no. 334906, and partly by a grant from the Ministry of Research, Innovation and Digitization, CNCS/CCDI-UEFISCDI, project number PN-IV-P6-6.3-SOL-2024-2-0220, within PNCDI IV.

Data. The detailed comparison reports between observed and predicted positions, with linked TDM files and the TLE orbital data, can be accessed from https://users.utcluj.ro/∼rdanescu/Flares/

REFERENCES

Ahmad, N., Herdiwijaya, D., Djamaluddin, T., Usui, H., Miyake, Y. (2018). Diagnosing low earth orbit satellite anomalies using NOAA-15 electron data associated with geomagnetic perturbations. *Earth Planets and Space*, 70, A 91.

Balan, M., Apostol, A.R., Cherciu, C., Turcu, V., Nedelcu, A., Trelia, M.M., Mihai, S.-S. (2022). Synoptes – Precise GNSS Timestamping Device for Space Surveillance and Tracking Operations. *Proceedings 73rd International Astronautical Congress 2022, 20th IAA Symposium on Space Debris (A6), Paris, France*, 22, Paper ID: 68551, 2022b. URL: https://iafastro.directory/iac/paper/id/68551/abstract-pdf/IAC-22,A6,IP,20,x68551.brief.pdf?2022-04-05.10:50:40. (Accessed July 14, 2025).

Baruah, Y., Roy, S., Sinha, S., Palmerio, E., Pal, S., Oliveira, D. M., Nandy, D. (2024). The loss of Starlink satellites in February 2022: How moderate geomagnetic storms can adversely affect assets in low-earth orbit. *Space Weather*, 22, e2023SW003716.

Brandt, D. A., Bussy-Virat, C. D., Ridley, A. J. (2020). A Simple Method for Correcting Empirical Model Densities During Geomagnetic Storms Using Satellite Orbit Data. *Space Weather*, Volume 18, Issue 12, article id. e02565.

Danescu, R., Itu, R., Fuzes, A., Turcu, V. (2024). Increasing the accuracy of real time wide field of view space surveillance by grid-based combination of multiple calibration results. *Advances in Space Research*, 73, 2098-2118.

Danescu, R., Itu, R., Muresan, M.P., Rednic, A., Turcu, V. (2022). SST Anywhere – A Portable Solution for Wide Field Low Earth Orbit Surveillance. *Remote Sensing*, 14, A 1905.

Gopalswamy, N., Xie, H., Yashiro, S., Akiyama, S. (2023). The solar cause of the 2022 February 3 geomagnetic storm that led to the demise of the Starlink satellites. *Sun and Geosphere*, 15, 65-74.

Kataoka, R., Shiota, D., Fujiwara, H., Jin, H., Tao, C., Shinagawa, H., Miyoshi, Y. (2022). Unexpected space weather causing the reentry of 38 Starlink satellites in February 2022. *Journal of Space Weather and Space Climate*, 12, A 41.

Kwak, Y.-S., Kim, J.-H., Kim, S., Miyashita, Y., Yang, T., Park, S.-H., Lim, E.-K., Jung, J., Kam, H., Lee, J., Lee, H., Yoo, J.-H., Lee, H., Kwon, R.-Y., Seough, J., Nam, U.-W., Lee, W. K., Hong, J., Sohn, J., Kwak, J. (2024). Observational Overview of the May 2024 G5-Level Geomagnetic Storm: From Solar Eruptions to Terrestrial Consequences. *Journal of Astronomy and Space Sciences*, vol. 41, issue 3, pp. 171-194.

Lang, D., Hogg, D. W., Mierle, K., Blanton, M., Roweis, S. (2010). Astrometry.net: Blind astrometric calibration of arbitrary astronomical images. *The Astronomical Journal*, 139, 1782-1800.

Miteva, R., Samwel, S.W., Tkatchova, S. (2023). Space Weather Effects on Satellites. *Astronomy*, 2, 165-179.

Motlaghzadeh, S., Vasiuta, M., Bister, M., Navarro Trastoy, A., Tuppi, L., Mayer-Gürr, T., Järvinen, H. (2024). Weather-induced satellite orbit perturbations. *Journal of Geophysical Research: Atmospheres*, 129, e2023JD040009.

NOAA Space Weather Prediction Center (2025). Solar cycle progression. URL: https://www.swpc.noaa.gov/products/solar-cycle-progression. (Accessed July 14, 2025).

Nwankwo, V.U., Chakrabarti, S.K., Weigel, R.S. (2015). Effects of plasma drag on low Earth orbiting satellites due to solar forcing induced perturbations and heating. *Advances in Space Research*, 56, 47-56.

Oliveira, D. M., Zesta, E. (2019). Satellite Orbital Drag During Magnetic Storms. *Space Weather*, Volume 17, Issue 11, pp. 1510-1533.

Orekit (2024). Orekit – An accurate and efficient core layer for space flight dynamics applications. URL: www.orekit.org. (Accessed July 14, 2025).

Parker, W.E., Linares, R. (2024). Satellite Drag Analysis During the May 2024 Gannon Geomagnetic Storm. *Journal of Spacecraft and Rockets*, 61, 1412-1415.

PlaneWave Instruments (2019a). L-500/L-600 Mechanical Installation Guide. URL: https://planewave.com/all-downloads/. (Accessed July 14, 2025).

PlaneWave Instruments (2019b). PlaneWave Interface 4 (PWI4) Software User Manual. URL: https://planewave.com/software-updates/. (Accessed July 14, 2025).

Pratiwi, N., Herdiwijaya, D., Ahmad, N., Hidayat, T., Ikhsan, M.I., Dina, D.F., Kusumawardani, P., Syamsurijal, Risnando, A., Rohmah, F. (2025). The effects of May 2024 solar and geomagnetic storms on an Indonesian GEO satellite's orbital parameters. *Advances in Space Research*, doi: https://doi.org/10.1016/j.asr.2025.07.021.

SBIG Astronomical Instruments (2015). Operating Manual STT Series CCD Cameras. URL: https://cdn.diffractionlimited.com/downloads/legacy/stt_manual_080112b.pdf?_gl=1*gg54c*_gcl_au*MTUyOTc1ODY4My4xNzI3ODg4NDg2*_ga*NzU2NDA1OTQuMTY2NDE3OTk2NA..*_ga_YE0GZQQRLK*MTcyODIxNDA5MS4yNS4xLjE3MjgyMTQ0MDguNjAuMC4w. (Accessed July 14, 2025).

Solar Influences Data Analysis Center – Royal Observatory of Belgium (2025) URL: https://sidc.be/article/gnss-impacts-10-11-may-extreme-storm. (Accessed July 14, 2025).

Vallado, D.A. (2013). Fundamentals of Astrodynamics and Applications. Fourth Edition, Microcosm Press, Hawthorne, CA, USA.

*Received on **